Proceedings of the ASME 2024
Pressure Vessels & Piping Conference
PVP2024
July 29 – August 2, 2024, Bellevue, WA, USA

PVP2024-122545

HYDROGEN EMBRITTLEMENT SUSCEPTIBILITY AND FRACTURE TOUGHNESS MEASUREMENTS OF WELDED X65M PIPELINE STEELS

Newell Moser[1], Zachary Buck[1], Nicholas Derimow[1], May L. Martin[1], Damian Lauria[1], Enrico Lucon[1], Peter Bradley[1], Matthew Connolly[1]

[1]National Institute of Standards and Technology (NIST), Boulder, CO, USA

ABSTRACT

Hydrogen is known to deteriorate the mechanical performance of steels (i.e., hydrogen embrittlement). The welding processes involved in the manufacturing and joining of steel pipelines locally modifies the microstructure of the steel, further complicating the situation. NIST has evaluated three steel pipes from industrial contacts to assess the susceptibility of seam welds to hydrogen embrittlement; these three pipes are made from API 5L X65M steel. The three steels were characterized in terms of microstructure, Charpy experiments (performed in air), and fracture toughness via single-edge notched bend specimens (performed in pressurized hydrogen). When testing in air, there was an apparent reduction in toughness for welded regions relative to the baseline steel. In hydrogen, a significant reduction in toughness was observed, however, the welded regions were the toughest. Microstructural differences in the welded region, namely grain size and the presence of phases like bainite, likely have the largest influence on these toughness differences.

Keywords: hydrogen, weld, fracture, piping

1. INTRODUCTION

The effect of global warming, combined with the economic challenges of driving the energy market's shift towards renewable energies, has made hydrogen an attractive energy carrier [1]. Geographic regions with high renewable energy supply (e.g., wind, solar, hydro-electric) are often geographically isolated and require energy carriers for storage and distribution to regions of high demand. Hydrogen gas (H2) is the most energy dense (by mass) and cleanest burning fuel in terms of carbon emissions, making H2 a critical emerging energy carrier. However, many structural materials, such as steels, are susceptible to hydrogen embrittlement, which can severely limit the service lifetime and fracture toughness of components made of such materials [2]. The degradation of mechanical properties of steel exposed to hydrogen was first recognized over a century ago by Johnson [3]. Johnson reported significant decreases in both the fracture toughness and breaking strain, but also noted that these effects were reversible when the steels were removed from the hydrogen environment. This phenomenon, now known broadly as "hydrogen embrittlement," is generally found in many structural metals, including the ferritic steels primarily used for long-distance pipelines as well as storage pressure vessels.

The relevant section from ASME B31.12 for qualifying steels (including welds) for hydrogen service is ASME B31.12 PL-3.7.1 [3]. The ASME B31.12 code on Hydrogen Piping and Pipelines provides two design principles for components exposed to H2. Option A is more conservative, limiting the design pressure and imposing a design penalty which ultimately increases the thickness of pipeline walls and therefore the amount of steel required. Option B provides a pathway to increase the pipeline design pressure. However, this option requires expensive and time-consuming fracture toughness and fatigue crack growth rate tests in high pressure H2 gas. Although Option B exists, the testing involved is rigorous, costly, and therefore not often implemented by end users.

To strike a balance between costly measurements and conservative design principles, there is considerable interest to provide a third option, Option C, within ASME B31.12 to allow for increased operating pressure. This approach is based on both fatigue and fracture toughness data collected since the modification to the code in 2019. Considering steels with a large range of microstructures, the fatigue and fracture performance in hydrogen can be further characterized by the in-air ductility attributes (the Charpy transition curves and the fracture toughness), the carbon equivalent, the maximum hardness, and the centerline segregation. In doing so, Option C would provide a suggested variety of microstructures that are shown to be least susceptible to degradation by hydrogen.

Towards this goal, it is critical to collect data on a wide range of pipeline steels and their welds. Hydrogen has been observed to have a severe effect on the fracture toughness of steels, with a

significantly larger effect in the weld heat-affected zone (HAZ) [4]. In general, the presence of hydrogen reduces the fracture toughness by at least a factor of two in modern steels when the gas pressure is 5.5 MPa or higher. On electro-chemically charged specimens examined by Alvarez et al., a ferrite-pearlite microstructure was observed to have a small decrease in fracture toughness in hydrogen, while a large decrease was observed for a ferrite-martensite microstructure [5]. It is not clear from current research whether yield strength and fracture toughness are correlated, and the fact that a range of microstructures can lead to similar yield strengths, but differing degrees of hydrogen susceptibility, further complicates this relationship [6,7].

ASME B31.12 non-mandatory Appendix G provides a guideline for producing steels with higher fracture toughness in hydrogen gas, based on the work done at ORNL and SECAT with testing from Sandia, NIST, and PowerTech labs [8]. These recommendations include limiting the carbon content (and carbon equivalent), microalloying with niobium, limiting the centerline segregation during continuous casting, using thermo-mechanical control processing, and producing a steel with a grain size of ASTM M-9.0 or finer [9]. These recommendations were made primarily with base metals in mind; the welding process complicates the guidelines in the non-mandatory Appendix G of ASME B31.12. While a given steel may start with a fine-grained, homogeneous microstructure (i.e., the base metal), high heat inputs during the welding process can produce coarse grained heat-affected zones (HAZ) that are well known to be among the worst microstructures for hydrogen susceptibility.

In this work, the chemistry and microstructure of three API PSL-2 X65M line pipe base metals, and their seam welds, are reported along with their performance in hydrogen as determined by ASTM E1820 fracture toughness testing. One of these base metals (Material A) follows all guidelines from the ASME B31.12 non-mandatory appendix G, another (Material C) follows all guidelines except the limitation on the carbon content, and the last (Material B) follows all guidelines except the limitation on carbon content and the limitation on the critical metal parameter (Pcm).

2. MATERIALS AND METHODS

Throughout this work, the three pipeline steels that were investigated will be anonymized using names Material A, Material B, and Material C. These three steels are represented in the construction of modern pipelines, and each of these line pipes were donated from industry collaborators for this study. More specifically, Material A was provided by one manufacturer, while Materials B and C were both provided by a second manufacturer. Moreover, these materials were never in-service. All three are classified as X65M steels with the nominal mechanical properties and dimensions of the pipelines provided in Table 1. During the manufacturing process, each pipe was seam welded using longitudinal submerged arc welding (SAW). For all three materials, the chemical compositions of the base-metal are given in Table 2 – the "baseline", or base, material corresponds to the metal far away from the weld region.

2.1 Micro-Hardness Mapping

Planar Vickers micro-hardness maps were generated using a digitally automated micro-hardness tester in accordance with ASTM E92-23 [10]. Excised cross-sections of the weld regions were hot mounted in conductive phenol-formaldehyde resin, and then polished, prior to micro-hardness mapping. Images were taken of these metallographic specimens using conventional optical (light) microscope imaging. Additional details about polishing and imaging are discussed in Section 2.2. After imaging, hardness maps were generated for each specimen. The total maximum load force was 0.5 kgf, and each indentation was held for 13 seconds. Successive indentations were separated by an approximate distance of 0.35 mm ± 0.05 mm, and the

TABLE 1: NOMINAL MECHANICAL PROPERTIES AND PIPELINE DIMENSIONS OF THE THREE MATERIALS.

	Material A	Material B	Material C
Steel Grade	API 5L X65M	API 5L X65M	API 5L X65M
Poisson's Ratio	0.30	0.30	0.30
Young's Modulus	210 GPa	210 GPa	210 GPa
Yield Strength	501 MPa	530 MPa	516 MPa
Ult. Tensile Strength	609 MPa	641 MPa	614 MPa
Wall Thickness	9.53 mm	19.05 mm	12.70 mm
Outer Diameter	762 mm	914 mm	762 mm

TABLE 2: CHEMICAL COMPOSITIONS IN WT %, INCLUDING THE CRITICAL METAL PARAMETER (Pcm). THE LAST COLUMN, App. G, SUMMARIZES WHETHER A GIVEN MATERIAL PASSED CONDITIONS (A), (B), AND/OR (C) FROM APPENDIX G OF ASME B31.12. CONDITION (A) STATES THAT CARBON CONTENT IS NOT TO EXCEED 0.07 WT %. CONDITION (B) STATES THAT THE STEEL SHALL BE ALLOYED WITH NIOBIUM. CONDITION (C) STATES THAT Pcm SHALL BE LESS THAN 0.17 (FOR API 5L X65 STEELS).

	C	Si	Mn	P	S	V	Nb	Ti	B	Pcm	App. G
Mat. A	0.06	0.29	1.36	0.009	0.001	0.006	0.041	0.016	0.0001	0.164	A, B, C
Mat. B	0.08	0.30	1.52	0.011	0.005	0.074	0.030	0.013	0.0002	0.180	B
Mat. C	0.08	0.30	1.47	0.016	0.003	0.071	0.027	0.015	0.0005	0.170	B, C

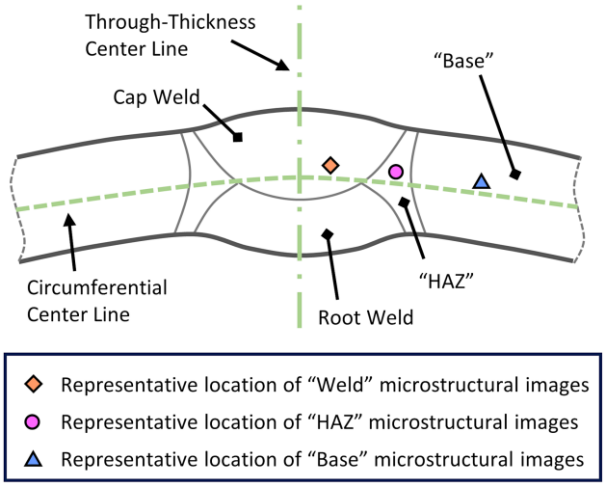

FIGURE 1: ANNOTATED DIAGRAM OF THE CROSS SECTION OF A SEAM WELD THAT ILLUSTRATES WHERE OPTICAL MICROSCOPY IMAGES WERE TAKEN TO CHARACTERIZE THE MICROSTRUCTURE. NOT DRAWN TO SCALE.

diagonals of the indentation – D1 and D2 – typically ranged between 0.045 mm and 0.065 mm.

2.2 Microstructural Analysis

Metallographic specimens for each condition were prepared by sectioning a portion of the pipes such that the representative regions of the weld-metal, HAZ, and base-metal could be hot mounted in conductive phenol-formaldehyde resin, commonly referred to as Bakelite. The mounted specimens were then ground to 320, 400, 600, 800, and 1200 grit with SiC paper, polished with 1 µm diamond suspension, and vibratory polished for 24 hours in colloidal silica. The specimens were etched in 5% Nital solution for 10 s prior to optical (light) microscope imaging. Representative microstructural images were taken of the base-metal, HAZ, and weld-metal for each steel, which are discussed later in Section 3.2. The relative locations of these optical images are illustrated in Figure 1.

2.3 Charpy Experiments

Charpy impact tests were performed in air for all three steels over a range of temperatures, which not only provides insight into the notch toughness of each material (quantified by the absorbed energy), but also highlights the ductile-to-brittle transition temperatures. Charpy specimens were notched to characterize three different regions with respect to the seam welds, see Figure 2 and caption: 1) the base-metal far away from the weld, 2) the HAZ outside of fusion line, and 3) the weld-metal along the center line of the weld.

Two sizes of the Charpy geometry were considered in this study, as shown in Figure 3 and elaborated in Table 3. The first is a standard geometry in accordance with ASTM E23-23a [11], and the second is a miniaturized Charpy geometry specifically chosen for Material A, which is defined in ASTM E2248-18 [12]. Due to the reduced wall thickness of Material A, there was insufficient material available to excise standard-sized Charpy specimens. The miniaturized Charpy specimen will be referred to as RHS for Reduced Half-Size. Additional details about this miniaturized Charpy geometry can be found in previous publications [13,14].

Charpy impact tests were performed at temperatures ranging from -196 °C to 150 °C. In the case of the standard specimens, an identical steel specimen instrumented with a T-type thermocouple, immersed in the same temperature conditioning medium, was used to monitor the test temperature. For RHS specimens, a K-type thermocouple attached to the test specimen was used to measure its actual temperature at impact. The overall precision of the temperature measurements is estimated to be ±3 °C. For test temperatures between -196 °C and -80 °C, liquid nitrogen was used to cool specimens, while between -80 °C and 21 °C, specimens were cooled in ethyl alcohol prior to transferring them to the impact position within approximately 3 s. For tests above room temperature, an electric hot plate was used to heat the specimens. For miniaturized Charpy specimens, a small-scale Charpy machine was utilized, with a capacity (potential energy) of 50.8 J. The impact velocity and radius of

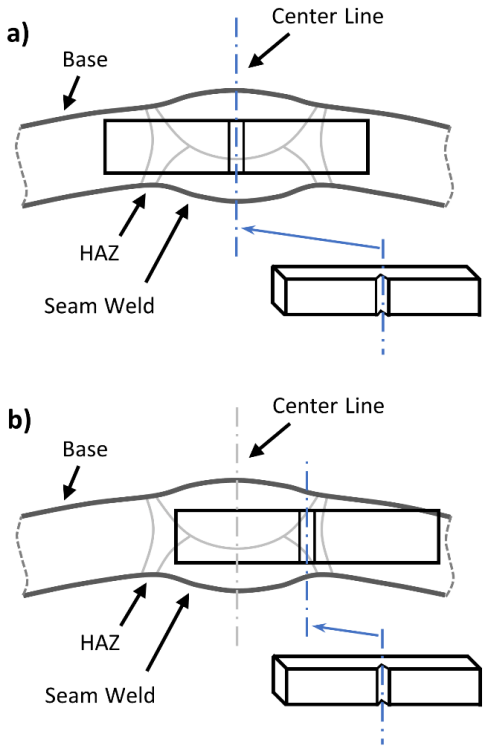

FIGURE 2: ANNOTATED DIAGRAM OF THE CROSS SECTION OF A SEAM WELD THAT ILLUSTRATES HOW CHARPY SPECIMENS WERE EXCISED FROM THE PIPELINE SAMPLES. a) "WELD" SPECIMENS WERE POSITIONED WITH THE CHARPY NOTCH PARALLEL TO THE FUSION LINE. b) "HAZ" SPECIMENS SAMPLED THE HEAT-AFFECTED ZONE WHICH IS LOCATED ON EITHER SIDE OF FUSION LINE. SPECIMENS THAT SAMPLED THE BASELINE MATERIAL, OR "BASE" MATERIAL, WERE TAKEN FAR AWAY FROM THE WELD. THE POSITIONS AND ORIENTATIONS OF THE SINGLE-EDGE NOTCHED BEND SPECIMENS WERE THE SAME AS THE CHARPY SPECIMENS. NOT DRAWN TO SCALE.

the striking edge of the small-scale machine were 3.5 m/s and 3.86 mm, respectively. For the standard Charpy specimens, a high-capacity machine was utilized, which has a potential energy of 953.6 J. The impact velocity and radius of the striking edge of the large-scale machine were 5.5 m/s and 8 mm, respectively.

2.4 Fracture Toughness

Fracture toughness tests were performed on the weld-metal in accordance to ASTM E1820-23 [15]. Single-edge notched bend, SE(B), specimens were tested in 207 bar (20.7 MPa) ultra-high pure hydrogen gas (99.999% pure). Specimens were machined with a geometry according to the ASTM E1820-23 standard with a nominal width (W) of 15.88 mm, as shown in Figure 4. Similar to the Charpy experiments, samples were oriented with the crack propagation direction along the weld, and the loading direction in the transverse direction (see Figure 2). Samples were pre-cracked in air at room temperature with the load ratio equal to 0.1 and the loading frequency set to 10 Hz.

The fracture toughness was determined from J-integral resistance curves (J-R curves). Crack mouth opening displacements (CMOD) were measured using a strain-gaged extensometer. The load was monitored using a 44 kN load cell mounted inside the pressure chamber. Elastic compliance was evaluated from the slope of the unloading portion of unloading-reloading cycles, which were performed at regular displacement intervals. The fracture toughness, J_Q, is defined as the intersection of the J-R curve with the 0.2 mm offset construction line; the construction lines have slopes equal to $2\sigma_y$ where σ_y is the average of the yield strength and ultimate tensile strength.

TABLE 3: NOMINAL DIMENSIONS (IN MM) OF THE STANDARD (Std.) AND MINIATURIZED (RHS) CHARPY SPECIMENS. THESE DIMENSIONS ARE SHOWN IN FIGURE 3. A MINIATURIZED GEOMETRY WAS CHOSEN FOR MATERIAL A DUE TO ITS REDUCED WALL THICKNESS. THE STANDARD GEOMETRY WAS CHOSEN FOR BOTH MATERIALS B AND C.

(mm)	L	W	B	R	N
Std.	55.00	10.00	10.00	0.25	2.00
RHS	24.13	4.83	4.83	0.13	0.97

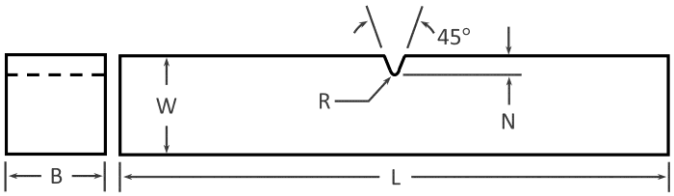

FIGURE 3: SIDE AND FRONT VIEWS OF THE CHARPY SPECIMEN. DIMENSIONS ARE GIVEN IN TABLE 3.

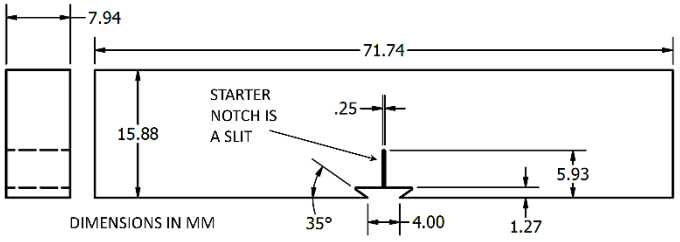

FIGURE 4: NOMINAL DIMENSIONS OF THE SINGLE-EDGE NOTCHED BEND, SE(B), SPECIMEN. SIDE AND FRONT VIEWS ARE ILLUSTRATED.

3. RESULTS AND DISCUSSION

3.1 Micro-Hardness Mapping

In addition to the etched cross-sections, the Vickers hardness maps for each material are shown in Figure 5. From the optical micrographs of the etched surfaces, there is a clear distinction between the roots and caps of the seam welds. In the weld regions, prior austenite grain boundaries are observed. Generally, reducing prior austenite grain size improves (mechanical) performance. However, contradictory results are often observed in the presence of hydrogen, possibly due to other factors such as alloying elements, H2 absorption, and dislocation density. The microstructure and grain size within these weld regions are discussed in Section 3.2.

The HAZ, located just outside of the fusion lines, is a transitional region containing recrystallized grains, grain growth, partially transformed zones, and tempered zones. Referring to Figure 5, the lowest hardness values are generally located within the tempered regions of HAZ – this is particularly evident for Materials B and C which have distinct, dark-blue rings in the hardness maps outside of their respective weld regions. Although the hardness values vary from material to material (see Figure 6), in all cases, the minimum hardness values are reduced by approximately 20 % in the HAZ with respect to base material.

For these welds, the filler material is either matched or overmatched to the base-metal with respect to tensile strength. Therefore, as expected, the hardness does not vary markedly (on average) in the weld region with respect to the base-metal. However, the hardness within the weld regions is not uniform nor symmetric; there are notable instances where the hardness within the weld region is significantly higher than the baseline material. This is evident upon noting the minimum and maximum hardness shown in Figure 6. Therefore, when characterizing the hardness of welded joints, it is important to consider a hardness map of the entire region encompassing a weld, not just a line-scan that crosses between the base-metal, HAZ, and weld-metal regions. Otherwise, important statistics, like peak hardness values, may go unnoticed.

3.2 Microstructural Analysis

Representative regions of the microstructures corresponding to base-metal, HAZ, and weld-metal regions can be seen in Figure 7 – recall that Figure 1 depicts the relative locations of these optical images.

Equiaxed α phase (i.e., ferrite), as well as small regions of bainitic microstructure, are observed in the base-metal regions for all three materials. In Material C, some areas also contain what appear to be localized regions of pearlite, as well as upper- and lower bainite. The mean grain size number calculation, per ASTM E112 Grain size number (or G_{avg}), within the base metal regions for Material A was found to be 13.9 ± 1.7; within the

baseline regions for Material B, G_{avg} was found to be 14.6 ± 1.6; within the baseline regions for Material C, G_{avg} was found to be 14.3 ± 1.7.

Similar to the baseline regions, equiaxed α phases and bainitic microstructures can also be found in the HAZ regions. However, closer to the weld region, coarsened α grains can be observed. Within the HAZ region for Material A, G_{avg} was found

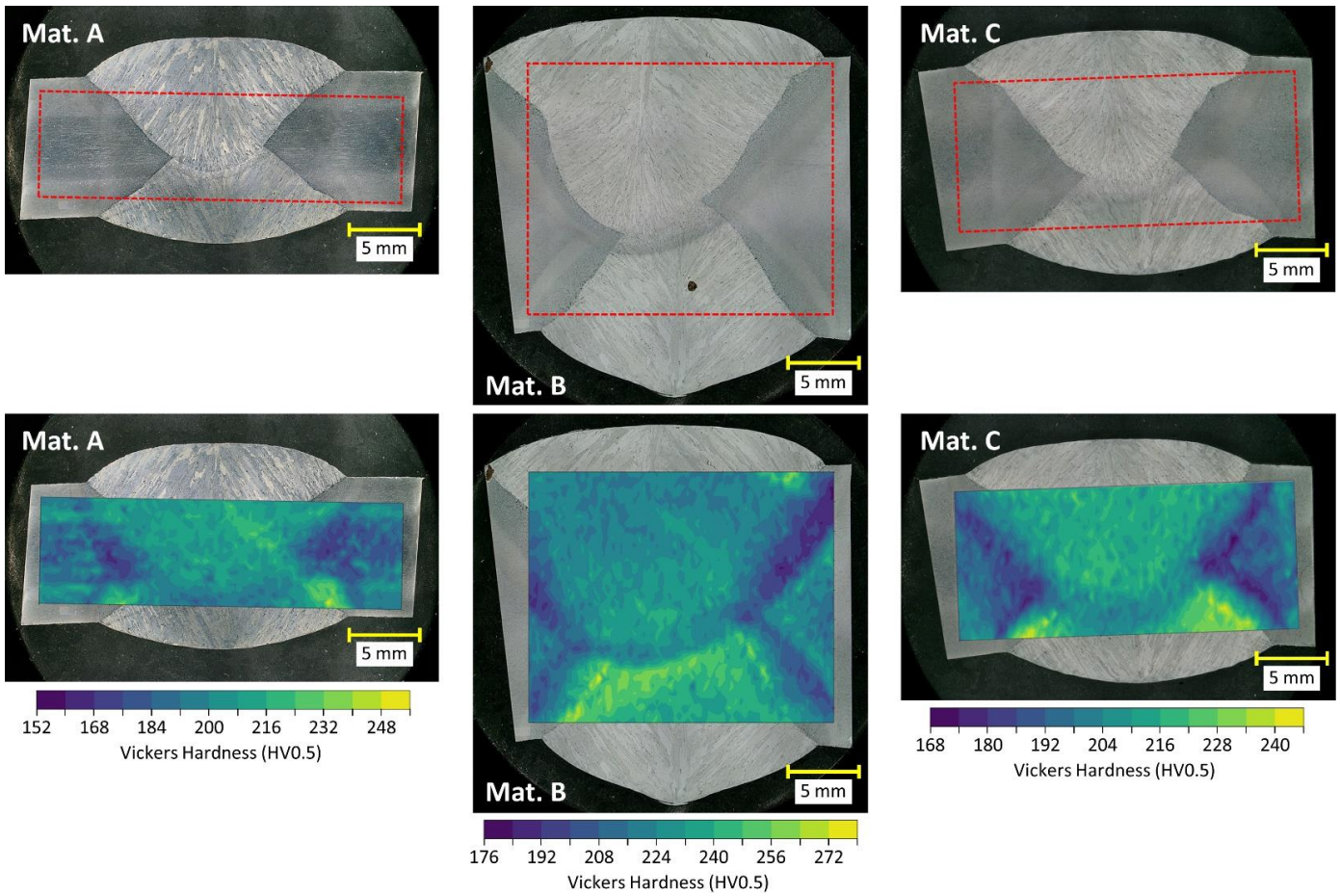

FIGURE 5: OPTICAL MICROGRAPHS OF THE ETCHED WELDS FOR MATERIALS A, B, AND C ARE SHOWN ALONG THE TOP ROW. THE DASHED RECTANGULAR BOX CORRESPONDS TO THE PERIMETERS OF THE VICKERS HARDNESS MAPS, WHICH ARE SHOWN ALONG THE BOTTOM ROW.

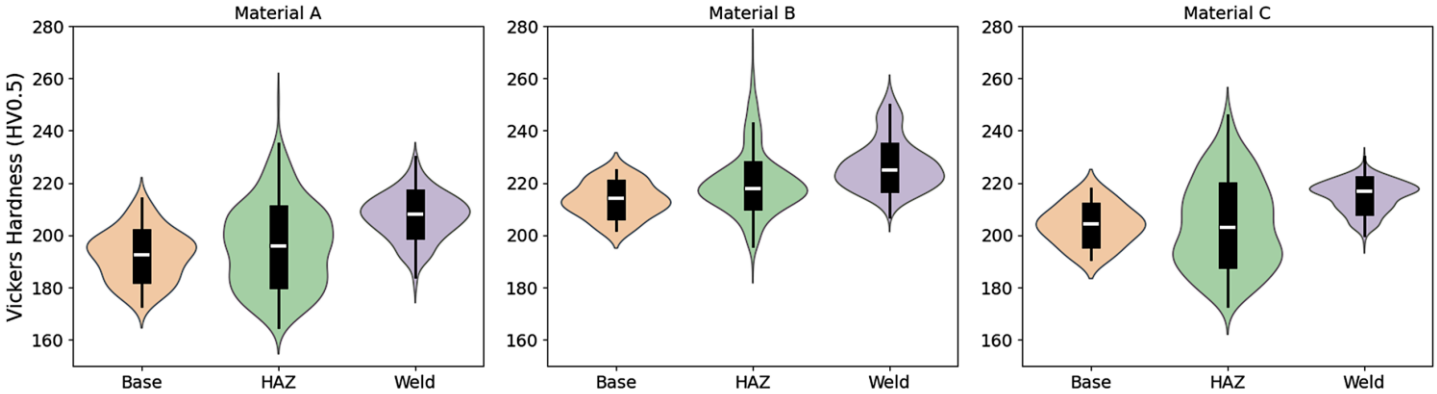

FIGURE 6: THE DISTRIBUTIONS OF VICKERS HARDNESS VALUES ARE ILLUSTRATED AS VIOLIN PLOTS FOR BASE, HAZ, AND WELD REGIONS. FOR EACH PLOT, THE WHITE MIDDLE-LINE REPRESENTS THE MEDIAN, THE THICK BAR REPRESENTS THE INTERQUARTILE RANGE, THE THIN LINE EXTENDING FROM THE THICK BAR REPRESENTS THE 1.5X INTERQUARTILE RANGE, AND THE WIDTH OF THE COLORED REGION REPRESENTS THE PROBABILITY DENSITY OF THE HARDNESS VALUES.

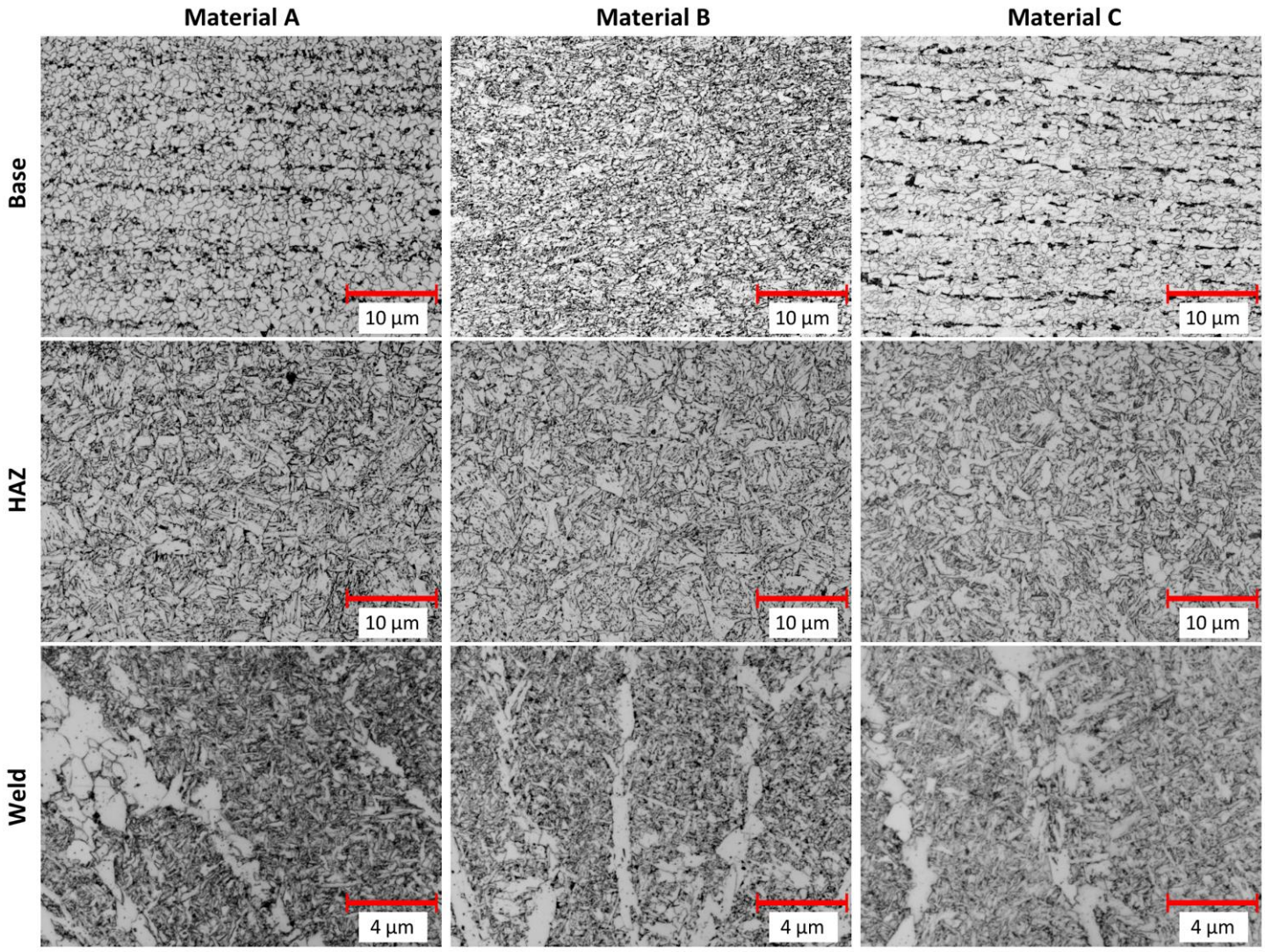

FIGURE 7: REPRESENTATIVE, ETCHED REGIONS OF THE "BASE, "HAZ", AND "WELD" MICROSTRUCTURES ARE SHOWN FOR EACH MATERIAL USING OPTICAL MICROSCOPY. THE RELATIVE LOCATIONS OF THESE IMAGES ARE DEPICTED IN FIGURE 1.

to be 13.9 $\pm$ 2.3; within the HAZ region for Material B, G_{avg} was found to be 14.3 $\pm$ 2.2; within the HAZ region for Material C, G_{avg} was found to be 13.8 $\pm$ 2.2.

Prior austenite (γ) boundaries containing allotriomorphic ferrite can be clearly observed in the welds of all three steels. Moreover, small pockets of bainite can be found, as well as Widmanstätten ferrite. Within the weld region for Material A, G_{avg} was found to be 14.5 $\pm$ 1.9; within the weld region for Material B, G_{avg} was found to be 15.3 $\pm$ 1.4; within the weld region for Material C, G_{avg} was found to be 15.3 $\pm$ 1.5.

3.3 Charpy Experiments

The absorbed energies from Charpy experiments, performed in air, are shown in Figure 8. As a reminder, a miniaturized Charpy geometry was required for Material A, hence the lower absorbed energies relative to Materials B and C. While not applied here, correlation functions can be used to relate the absorbed energies between the different Charpy geometries [16]. Focusing on the upper-shelf energies, for all three steels, the absorbed energies of the Charpy specimens excised from weld regions were significantly smaller compared to those from the HAZ and base-metal regions. Moreover, for all three materials, the upper-shelf energies for the HAZ regions are similar to those of the base-metal. The ductile-to-brittle transition temperatures range between approximately -100 °C and 0 °C. The transition temperatures of the weld regions notably differ relative to the base and HAZ regions – the transition temperatures of the weld regions are higher relative to the base and HAZ regions.

3.4 Fracture Toughness

In the SE(B) experiments, a significant reduction in toughness was observed for all materials in 20.7 MPa hydrogen gas compared to in air. Valid ASTM E1820 tests are not possible for these materials in air due to the high ductility and limited wall thickness of the parent pipes. However, it is still clear from the

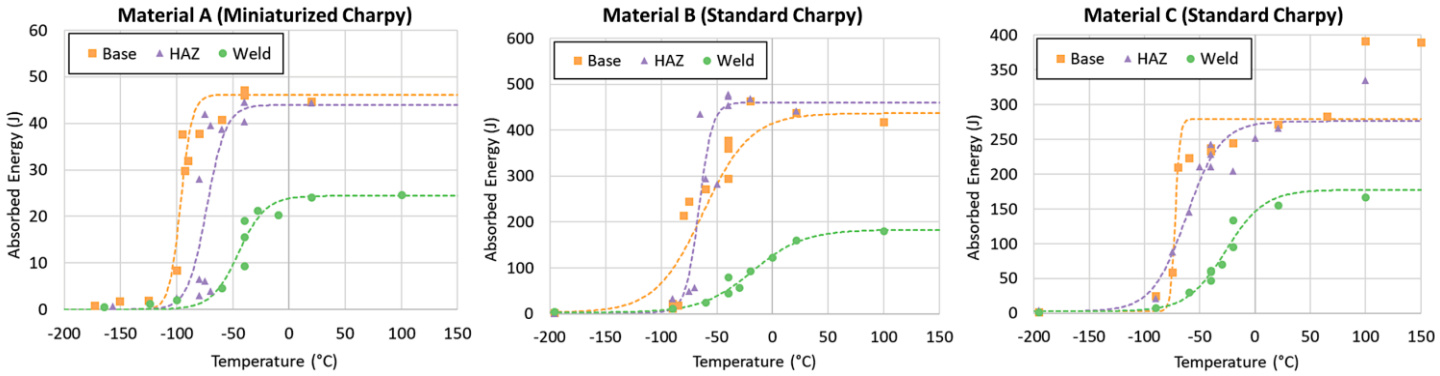

FIGURE 8: THE ABSORBED ENERGIES FROM CHARPY EXPERIMENTS PERFORMED (IN AIR) OVER A RANGE OF TEMPERATURES ARE SHOWN FOR EACH MATERIAL. THE DASHED LINES ARE FITTED CURVES FOLLOWING A HYPERBOLIC TANGENT MODEL. NOTE THE DIFFERENCE IN SCALES FOR THE ABSORBED-ENERGY Y-AXES. A MINIATURIZED CHARPY GEOMETRY WAS REQUIRED FOR MATERIAL A, HENCE THE LOWER ABSORBED ENERGIES.

data that the fracture toughness values of these materials are at least five times greater in air than in ultra-pure hydrogen.

Following ASTM E1820, a power-law was fitted to qualified points of the JR-curves; these measured JR-curves are shown in the Appendix. The J_Q toughness is defined as the intersection of this power-law with the 0.2 mm exclusion line. These J_Q values were converted to K_{JQ}, which is the classical fracture toughness in mode I. The averaged quantities of K_{JQ} among repeated experiments are shown in Figure 9. It is important to note that, due to the geometry of the welds and samples, the "HAZ" specimens not only sample across the HAZ,

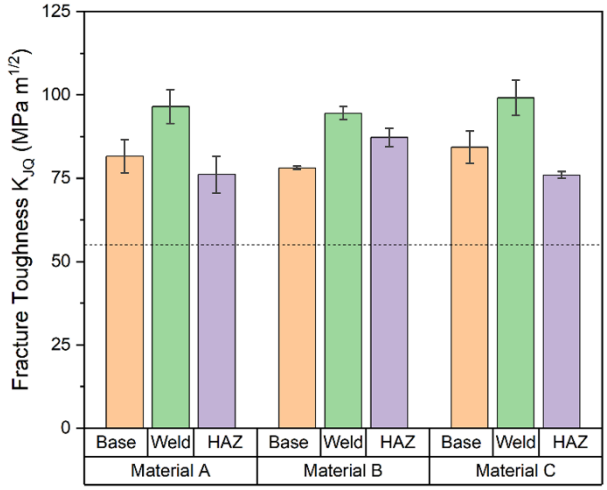

FIGURE 9: THE FRACTURE TOUGHNESS VALUES IN MODE I, K_{JQ}, ARE SHOWN, WHICH HAVE BEEN CONVERTED FROM J_Q IN ACCORDANCE WITH ASTM E1820. THE VALUES GIVEN HERE CORRESPOND TO TESTS PERFORMED IN A PURE HYDROGEN EVIRONMENT; EACH VALUE REPRESENTS THREE REPEATED, AVERAGED TESTS. THE ERROR BARS CORRESPOND TO ONE STANDARD DEVIATION AMONG REPEATED TESTS. THE DASHED REFERENCE LINE AT 55 MPa m$^{1/2}$ REPRESENTS THE ASME B31.12 MINIMUM FRACTURE TOUGHNESS IN HYDROGEN.

but they also likely include small contributions from the base metal and/or weld metal.

In general, the weld regions show the highest toughness in hydrogen when compared to the base and HAZ regions. The HAZ for Material A and Material C show lower toughness than the base and weld, while for Material B, the HAZ has higher toughness than the base metal. Interestingly, for Material B, the HAZ was also the toughest in air according to the Charpy experiments (see Figure 8).

3.5 Discussion

For the SE(B) experiments performed in hydrogen, the difference in the toughness values between the weld regions and the base/HAZ regions is significantly smaller relative to the spread in the absorbed energies from Charpy experiments. In fact, for each material, the highest toughness values were measured in the weld region when testing SE(B) specimens in hydrogen. Conversely, the weld region for each material had the lowest upper-shelf energies from the Charpy experiments, suggesting that in-air ductility properties are not necessarily correlated with in-hydrogen ductility.

For each of the base, weld, and HAZ regions, Material B had the highest hardness values compared to Materials A and C, and correspondingly, Material B had the lowest toughness in hydrogen when comparing similar weld regions for the other two materials. While the limited data seem to suggest a correlation between higher hardness and higher fracture toughness in hydrogen, the possible trend is subtle and within the standard deviation of the hardness measurements.

To reiterate, Material A follows all recommendations from non-mandatory Appendix G of ASME B31.12, Material B exceeds both the Pcm and carbon content suggested limits, and Material C exceeds only the carbon content suggested limit. However, Material C demonstrated the highest fracture toughness when comparing only the base-metal. Though the suggestions from non-mandatory Appendix G of ASME B31.12 are intended to produce a material with favorable microstructures for hydrogen service, Material A – which followed all suggestions – had coarser grains in the base metal

compared to the other two materials. Additionally, in the HAZ and weld section, a larger fraction of bainitic microstructure phase was observed. Both of these may explain the lower toughness compared to Materials B and C.

While there were some differences in fracture toughness between the three materials (see Appendix A), each of them has an in-hydrogen fracture toughness that exceeds the ASME B31.12 minimum of 55 MPa $m^{1/2}$ despite minor departures from the recommendations outlined in the non-mandatory Appendix G, specifically for Materials B and C.

4. CONCLUSION

While the ASME B31.12 standard provides guidance for the qualification of pipeline steels for hydrogen transport, the standard primarily targets the baseline properties of a given steel. Three pipeline steels, each classified as API 5L X65M, were studied in this work, and the mechanical performance of the welded regions were assessed under the influence of hydrogen. Each of the three materials were characterized in terms of microstructure, Charpy impact energy (in air), and SE(B) experiments (in hydrogen). Our conclusions are as follows,

- All three materials experienced a significant reduction in fracture toughness in hydrogen compared to in air. While fracture toughness values from SE(B) experiments (quantified as K_{JQ}) performed in air are uncertain due to size restrictions of the specimens, it is evident that the fracture toughness was reduced by at least a factor of five.
- Charpy upper-shelf energy, a measure of in-air ductility, does not appear to be correlated with the in-hydrogen ductility. Although the weld regions had significantly lower upper-shelf energies, the measured fracture toughness values (quantified as K_{JQ}) in the weld were higher than those in the base and HAZ.
- Microstructural differences, namely grain size and the presence of microstructural phases such as bainite, likely play a large role in the toughness of the material. While the non-mandatory ASME B31.12 Appendix G provides a guideline for generating a suitable microstructure for H2 service, small deviations from the recommendations in the materials studied here were not sufficient to substantially increase hydrogen susceptibility.

With this limited data set, we cannot in confidence suggest any modifications to ASME B31.12 Appendix G. In the future, we plan to expand on this research by investigating additional pipeline steels/grades, consider different welding conditions, and dive deeper into the relationships between microstructure, mechanical performance, and hydrogen susceptibility.

ACKNOWLEDGEMENTS

This work was supported by the Department of Transportation (DOT) Pipeline and Hazardous Materials Safety Administration (PHMSA), Contract # 693JK319N000013-02.

REFERENCES

[1] Obama, B., 2017, "The Irreversible Momentum of Clean Energy," Science, **355**(6321), pp. 126–129.

[2] Martin, M. L., Connolly, M. J., DelRio, F. W., and Slifka, A. J., 2020, "Hydrogen Embrittlement in Ferritic Steels," Applied Physics Reviews, **7**(4), p. 041301.

[3] 2023, *Hydrogen Piping and Pipelines B31.12*, ASME.

[4] Qu, Feng, An, Bi, Du, Yang, and Zheng, 2019, "Hydrogen-Assisted Crack Growth in the Heat-Affected Zone of X80 Steels during in Situ Hydrogen Charging," Materials, **12**(16), p. 2575.

[5] Álvarez, G., Peral, L. B., Rodríguez, C., García, T. E., and Belzunce, F. J., 2019, "Hydrogen Embrittlement of Structural Steels: Effect of the Displacement Rate on the Fracture Toughness of High-Pressure Hydrogen Pre-Charged Samples," International Journal of Hydrogen Energy, **44**(29), pp. 15634–15643.

[6] Stalheim, D., Boggess, T., Bromley, D., Jansto, S., and Ningileri, S., 2012, "Continued Microstructure and Mechanical Property Performance Evaluation of Commercial Grade API Pipeline Steels in High Pressure Gaseous Hydrogen," *Volume 3: Materials and Joining*, American Society of Mechanical Engineers, Calgary, Alberta, Canada, pp. 275–283.

[7] Stalheim, D., Boggess, T., San Marchi, C., Jansto, S., Somerday, B., Muralidharan, G., and Sofronis, P., 2010, "Microstructure and Mechanical Property Performance of Commercial Grade API Pipeline Steels in High Pressure Gaseous Hydrogen," *2010 8th International Pipeline Conference, Volume 2*, ASMEDC, Calgary, Alberta, Canada, pp. 529–537.

[8] Ningileri, S. T., Boggess, T. A., and Stalheim, D., 2013, *Materials Solutions for Hydrogen Delivery in Pipelines*, DOE/GO/15036, 1059020.

[9] 2021, *ASTM E112-13: Test Methods for Determining Average Grain Size*.

[10] 2023, "ASTM E92-23: Test Methods for Vickers Hardness and Knoop Hardness of Metallic Materials."

[11] 2023, *ASTM E23-23a: Standard Test Methods for Notched Bar Impact Testing of Metallic Materials*.

[12] 2018, *ASTM E2248-18: Standard Test Method for Impact Testing of Miniaturized Charpy V-Notch Specimens*.

[13] Lucon, E., McCowan, C. N., and Santoyo, R. L., 2015, *Impact Characterization of Line Pipe Steels by Means of Standard, Sub-Size and Miniaturized Charpy Specimens*, NIST TN 1865, NIST, Gaithersburg, MD.

[14] Lucon, E., and Hrabe, N., 2018, "Instrumented Impact Testing of Miniaturized Charpy Specimens of AM Ti-6Al-4V," Matls. Perf. Charact., **7**(1), p. 20170160.

[15] 2023, *ASTM E1820-23a: Standard Test Method for Measurement of Fracture Toughness*.

[16] Lucon, E., 2012, *Miniaturized Charpy Specimens for the Indirect Verification of Small-Scale Charpy Machines: Initial Qualification Phase*, TN 1562-1, NIST, Gaithersburg, MD.

APPENDIX

In accordance with ASTM E1820, the J-R curves from all of the SE(B) experiments are shown in Figure A1.

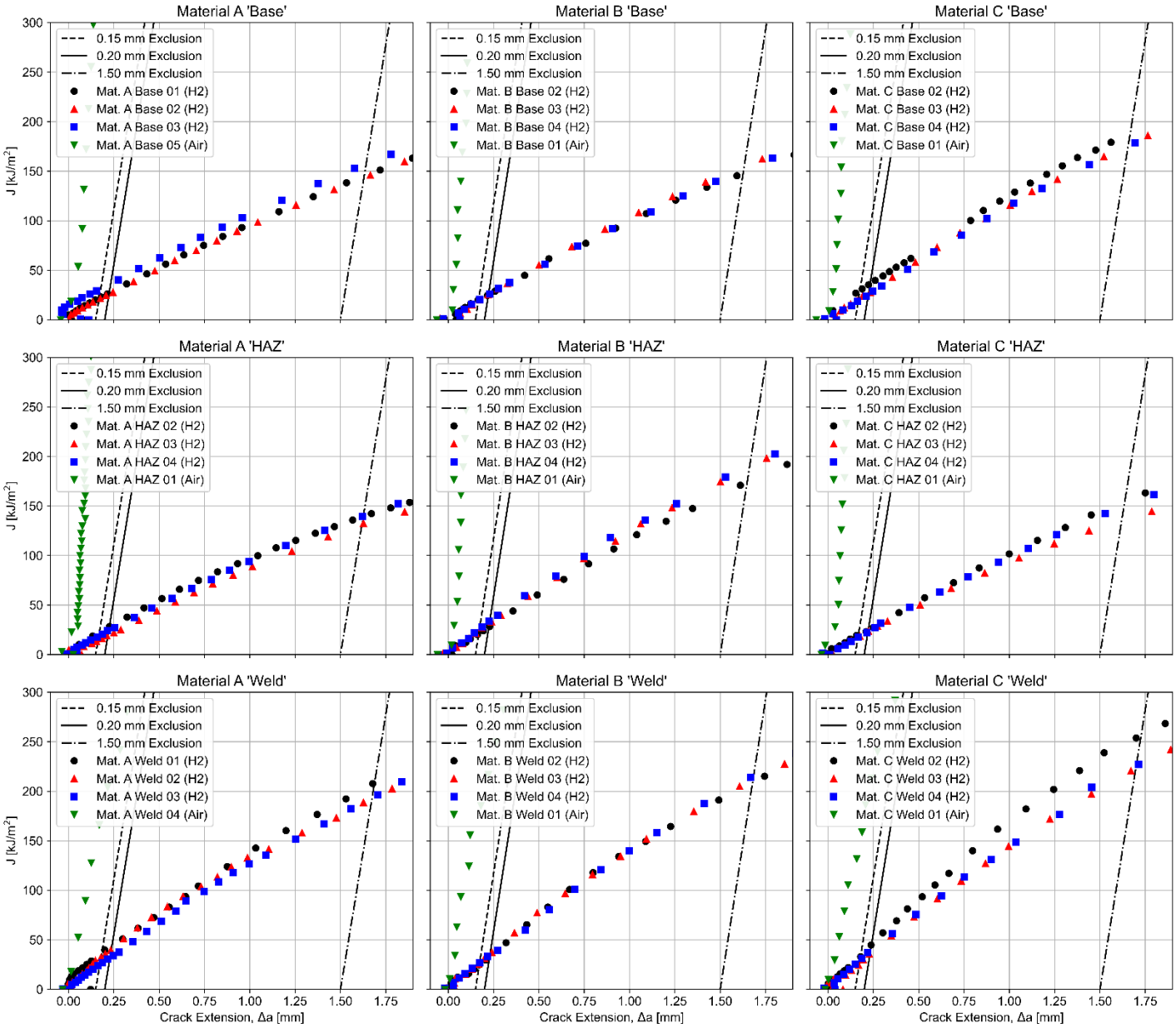

FIGURE A1: FRACTURE TOUGHNESS VALUES FROM THE SE(B) EXPERIMENTS, GIVEN AS J-R CURVES, ARE ILLUSTRATED FOR EACH MATERIAL. REPEATED TESTS WERE PERFORMED IN A PRESSURIZED HYDROGEN ENVIRONMENT, DENOTED AS "H2"; ALL MATERIALS WERE ALSO TESTED IN AIR, DENOTED AS "AIR". NOTE, ALMOST ALL OF THE EXPERIMENTS PERFORMED IN AIR RESULTED IN AN INVALID J_Q DUE TO THE EXCEEDINGLY HIGH DUCTILITY OF THE MATERIALS, COMBINED WITH THE LIMITED THICKNESS OF THE PARENT PIPES WHICH PROHIBITED PLANE STRAIN CONDITIONS.